NANO LETTERS

2007
Vol. 7, No. 10
3172−3176

Nanomechanical Characterization of One-Step Combustion-Synthesized $Al_4B_2O_9$ and $Al_{18}B_4O_{33}$ Nanowires

Xinyong Tao, Xinnan Wang, and Xiaodong Li*

Department of Mechanical Engineering, University of South Carolina, 300 Main Street, Columbia, South Carolina 29208

Received July 20, 2007

ABSTRACT

Two kinds of aluminum borate nanowires, $Al_4B_2O_9$ and $Al_{18}B_4O_{33}$, were successfully synthesized by a one-step combustion method through control of the Al:B atomic ratio and synthesis temperature. Both nanowires are single crystalline but have distinguishing growth habits. Nanoindentation tests were performed directly on individual nanowires to reveal their mechanical properties. A 70% reduction in elastic modulus was found in $Al_{18}B_4O_{33}$ nanowires compared with their bulk counterpart. $Al_{18}B_4O_{33}$ nanowires exhibited higher hardness and elastic modulus than $Al_4B_2O_9$ nanowires.

One-dimensional nanostructures, such as nanotubes, nanowires, and nanobelts, have attracted tremendous attention due to their applications in electronics, optics, and mechanics.[1−7] Aluminum borates are remarkable ceramic materials with excellent mechanical properties, good chemical inertness, high-temperature stability, and light weight as well as low thermal expansion coefficient.[8−16] Especially, aluminum borate nanowires possess great potential in nonlinear optical materials, oxidation-resistant, whisker-reinforced composites, and electronic ceramics.[8−15] Some aluminum borate nanowires including $Al_4B_2O_9$ and $Al_{18}B_4O_{33}$ have been synthesized via several approaches such as thermal evaporation,[8] sol−gel,[11] and chemical vapor deposition.[16] These methods usually need high temperature,[8] catalyst particles[16] or a series of steps.[11] Finding a controllable and cost-effective synthesis method remains a great challenge. Because of its low cost and high efficiency, the combustion synthesis method[17−19] has been mostly applied for producing complex oxide ceramics such as aluminates, ferrites, and chromites. Combustion synthesized powders are generally more homogeneous and have fewer impurities; the surface areas are higher than those of powders prepared by conventional solid-state methods.[17] However, no reports have been published on the synthesis of aluminum borate nanowires using the one-step combustion method. In this letter, we demonstrate that the one-step combustion technique can be used to grow aluminum borate nanowires. By tailoring the molar ratio of elements Al to B and synthesis temperature, high purity $Al_4B_2O_9$ and $Al_{18}B_4O_{33}$ nanowires can be obtained.

Compared with the well-established synthesis techniques for growing aluminum borate nanowires, their mechanical properties are still lacking in literature. This limits their practical applications in constructing aluminum borate nanowire based nanocomposites and functional nanodevices. Here we report, for the first time to our knowledge, the mechanical properties of individual $Al_4B_2O_9$ and $Al_{18}B_4O_{33}$ nanowires obtained using atomic force microscope (AFM) based nanoindentation technique. We found a 70% reduction in elastic modulus of $Al_{18}B_4O_{33}$ nanowires compared with their bulk counterpart. It was also proved that $Al_{18}B_4O_{33}$ nanowires had higher hardness and elastic modulus than $Al_4B_2O_9$ nanowires. These findings are significant for designing aluminum borate nanowire based nanocompsites and functional nanodevices.

The one-step combustion method was used to prepare the aluminum borate nanowires. The required proportions of $Al(NO_3)_3{\cdot}9H_2O$, H_3BO_3, NH_4NO_3, and $C_6H_8O_7{\cdot}H_2O$ were dissolved in the minimum amount of water in a crucible, which was then placed in a muffle furnace preheated to 900 or 1050 °C. Upon water evaporation, a combustion reaction took place according to theoretical redox reactions 1 and 2 to synthesize $Al_4B_2O_9$ and $Al_{18}B_4O_{33}$ nanowires, respectively:

$$0.4Al(NO_3)_3{\cdot}9H_2O + 1.2H_3BO_3 + 1.5NH_4NO_3 + 0.5C_6H_8O_7{\cdot}H_2O \xrightarrow{900\ ^\circ C} 0.1Al_4B_2O_9 + 0.5B_2O_3 + 3CO_2 + 10.9H_2O + 2.1N_2 \quad (1)$$

$$0.18Al(NO_3)_3{\cdot}9H_2O + 0.18H_3BO_3 + 0.9NH_4NO_3 + 0.25C_6H_8O_7{\cdot}H_2O \xrightarrow{1050\ ^\circ C} 0.01Al_{18}B_4O_{33} + 0.07B_2O_3 + 1.5CO_2 + 4.94H_2O + 1.17N_2 \quad (2)$$

* Author to whom correspondence should be addressed. E-mail: lixiao@engr.sc.edu. Web address: http://www.me.sc.edu/research/nano/.

10.1021/nl071772x CCC: $37.00
Published on Web 08/31/2007

The combustion was maintained for about 6 min. Loose white powders were obtained after 2 h annealing. All the solid powders were washed, filtered, and dried to get the final products.

The as-prepared powders were identified by X-ray diffraction (XRD). A few drops of nanowires containing ethanol solution were deposited onto copper grids or Si substrate for transmission electron microscopy (TEM, Hitachi H-8000), high-resolution transmission electron microscopy (HRTEM, JEOL JEM 2010F), energy dispersive X-ray spectroscopy (EDX), and nanoindentation (Hysitron, Triboscope nanoindenter) studies.

To avoid nanowire sliding during the nanoindentation tests, both ends of the nanowires to be tested were fixed through EBID[20] of paraffin in a scanning electron microscope (SEM, FEI Quanta 200). The cross-sectional TEM specimens were prepared by slicing nanowires embedded in Spurr's epoxy resin with a Sorvall Porter-Blum MT2-B ultramicrotome.

A Hysitron triboscope nanoindenter, in conjunction with the Veeco Dimension 3100 AFM, was used to perform imaging and in situ nanoindentation tests for mechanical property measurements. The Berkovich indenter monitored and recorded the load and displacement during indentation with a force resolution of about 1 nN and displacement resolution of about 0.2 nm.[21,22] The indenter tip was first used to image and locate a single nanowire and then in situ indent the nanowire. Post-test imaging provided the ability to verify that the test was performed in the anticipated location, which maximized the reliability of data and aids in explanation of unexpected test results. Hardness and elastic modulus were calculated from the load displacement curves. Before each nanoindentation test, the thermal drift was automatically tracked and recorded by means of introducing the nanoindenter in touch with the top surface of the sample with minimum contact load. All the nanoindentation tests were performed when the thermal drift or vibration induced mechanical drift dropped down to 0.01 nm/s. The load-displacement curves were obtained by subtracting the drift effect for hardness and elastic modulus analyses.

Figure 1a shows the XRD spectrum of the product synthesized with an Al:B atomic ratio of 1:3 at 900 °C for 2 h. All the diffraction peaks can be indexed to the orthorhombic phase of $Al_4B_2O_9$ with the lattice parameters of $a = 1.48$ nm, $b = 1.51$ nm, and $c = 0.56$ nm, which are in good agreement with the standard parameters (JCPDS 09-0158). No diffraction peaks of any impurity were observed in the XRD spectrum, indicating high purity of the final product. The TEM image in Figure 1b reveals that the product consists of abundant straight nanowires with diameter ranging from 50 to 200 nm. The surface of the nanowire is clean, and no any amorphous coatings can be found. The cross-sectional TEM image of the $Al_4B_2O_9$ nanowire (Figure 1c) shows an interesting octagonal structure including four large facets and four small facets. The polygonal plane in the cross section provides evidence of anisotropy for lateral crystal growth. It is well-known that the equilibrium shape of a free particle is determined by the surface energy. The surface energy is a function of the surface normal, $r(n)$, and

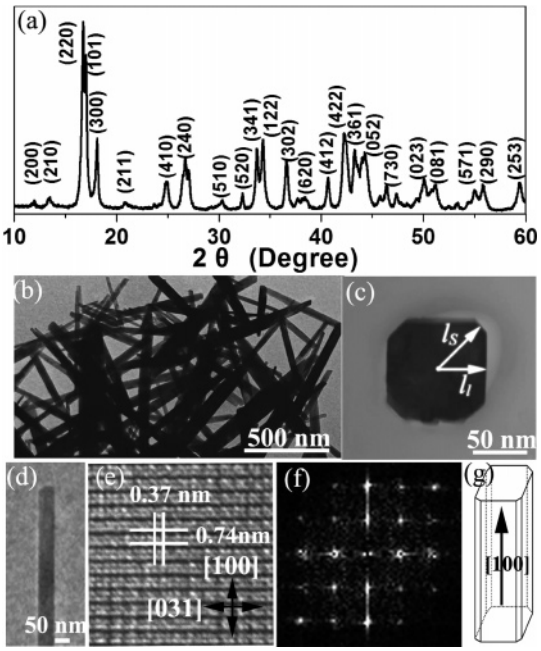

Figure 1. 1. (a) XRD spectrum of the product synthesized at 900 °C for 2 h. (b) Bright-field TEM image of $Al_4B_2O_9$ nanowires. (c) Cross-sectional TEM image of an $Al_4B_2O_9$ nanowire. (d) TEM, (e) HRTEM, and (f) corresponding fast Fourier transform (FFT) images of an $Al_4B_2O_9$ nanowire. (g) Schematic of the $Al_4B_2O_9$ nanowire growth.

for any element of the crystal surface, dA, the surface energy is $r(n)$ dA, where n is normal to the element dA. For a single crystal with fixed volume in thermodynamic equilibrium, the shape is that which minimizes the total surface energy, E:[23,24]

$$E = \int r(n)\, \mathrm{d}A \tag{3}$$

On the basis of eq 3, it has been demonstrated that, for a crystal in equilibrium, the ratio of the energies of two orientations (r_1 and r_2) is equal to the ratio of the perpendicular distances from the center of the crystal to the facet (l_1 and l_2):[23,24]

$$l_1/l_2 = r_1/r_2 \tag{4}$$

As shown in Figure 1c, the large facets are closer to the center of the crystal than the small facets ($l_l < l_s$). So it can be concluded that the small facets in $Al_4B_2O_9$ have higher surface energy than the large facets. Parts e and f of Figure 1 are the HRTEM image and corresponding FFT image of an $Al_4B_2O_9$ nanowire shown in Figure 1d. It can be found that the synthesized nanowire is single crystalline, and the axis direction of the $Al_4B_2O_9$ nanowire is along [100].

Figure 2a is the XRD spectrum of the product synthesized with an Al:B atomic ratio of 1:1 at 1050 °C for 2 h. The spectrum can be indexed to the orthorhombic phase of $Al_{18}B_4O_{33}$ with the lattice parameters of $a = 0.769$ nm, $b = 1.501$ nm, and $c = 0.566$ nm, which are in good agreement with the standard parameters (JCPDS 32-0003). No diffraction peaks from any impurity, such as Al_2O_3, B_2O_3 and

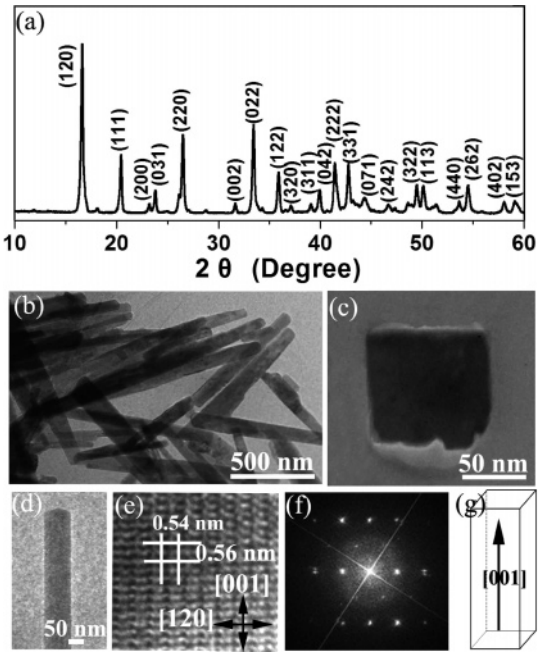

Figure 2. (a) XRD spectrum of the product synthesized at 1050 °C for 2 h. (b) Bright-field TEM image of $Al_{18}B_4O_{33}$ nanowires. (c) Cross-sectional TEM image of an $Al_{18}B_4O_{33}$ nanowire. (d) TEM, (e) HRTEM, and (f) corresponding FFT images of a single $Al_{18}B_4O_{33}$ nanowire. (g) Schematic of the $Al_{18}B_4O_{33}$ nanowire growth.

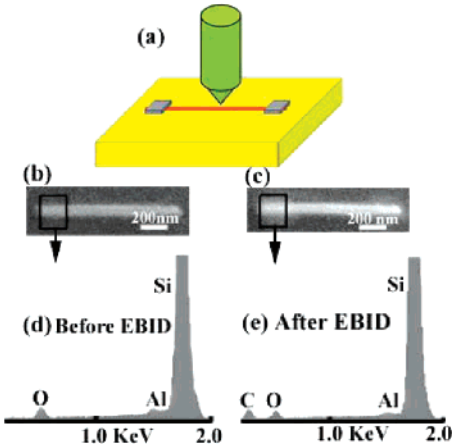

Figure 3. (a) Schematic of nanoindentation on a nanowire clamped to silicon substrate by EBID. (b−c) SEM images of a single aluminum borate nanowire before and after EBID, respectively. (d) EDX spectrum result from the rectangle area in (b) showing the almost absence carbon peak before EBID, and (e) EDX spectrum result from the rectangle area in (c) showing an obvious carbon peak, which indicates a carbon layer was successfully deposited onto the rectangle area after 15 min EBID.

$Al_4B_2O_9$, can be identified, indicating that high purity $Al_{18}B_4O_{33}$ instead of $Al_4B_2O_9$ has been successfully synthesized by changing the Al:B atomic ratio and growth temperature. The TEM image in Figure 2b shows abundant straight nanowires with diameter ranging from 80 to 250 nm. The cross-sectional TEM image (Figure 2c) suggests that the $Al_{18}B_4O_9$ nanowire has a nearly square structure, which is different from $Al_4B_2O_9$ nanowire (Figure 1c). No small facets with high surface energy exist in the cross-sectional TEM image of $Al_{18}B_4O_9$. The surface of $Al_{18}B_4O_9$ is rougher than $Al_4B_2O_9$, implying better crystallinity of $Al_4B_2O_9$ nanowires. The HRTEM image (Figure 2e) and corresponding FFT image (Figure 2f) illustrate that the synthesized nanowire is single crystalline, and the axis direction of the $Al_{18}B_4O_{33}$ nanowire is along [001].

To understand the difference of growth habits between $Al_4B_2O_9$ and $Al_{18}B_4O_9$ nanowires, a series of experiments focusing on the growth temperature (700−1100 °C) effect on the nanowires are performed. It was found that the minimum temperature required for the formation of $Al_4B_2O_9$ and $Al_{18}B_4O_{33}$ nanowires are 780 and 1020 °C, respectively. The growth temperature for the $Al_4B_2O_9$ nanowires shown in Figure 1 is 900 °C, which is considerably higher than the minimum required temperature 780 °C. But the synthesis temperature for the $Al_{18}B_4O_{33}$ nanowires shown in Figure 2 is 1050 °C, which is close to the minimum required temperature 1020 °C. It means that there is more energy for the growth of $Al_4B_2O_9$ nanowires than for the growth of $Al_{18}B_4O_{33}$ nanowires. This is why the $Al_4B_2O_9$ nanowires have better crystallinity than the $Al_{18}B_4O_{33}$ nanowires. Our extensive TEM analysis showed that no any metal impurities could be found on the tip of the nanowires, suggesting a self-catalytic growth mechanism.[11,25] It was also found that the H_3BO_3 must be excessive over the stoichiometry of $Al_4B_2O_9$ and $Al_{18}B_4O_{33}$, otherwise some Al_2O_3 particles will appear in the product.

To study the mechanical properties of $Al_4B_2O_9$ and $Al_{18}B_4O_{33}$ nanowires, a few drops of nanowires containing ethanol solution were deposited onto a clean Si substrate for the nanoindentation experiments. In our previous nanoindentation tests,[26−29] the EBID clamping method was not used to stabilize the nanostructures because there was good contact between the samples and the substrate. In this work, we found that the adhesion between aluminum borate nanowires and the Si substrate was weak, which results from the special shapes of these nanowires. So the EBID clamping method was introduced to avoid the sliding of the aluminum borate nanowires. Figure 3a is the schematic of nanoindentation on a nanowire fixed to a Si substrate by EBID. Parts b and c of Figure 3 show SEM images of a single aluminum borate nanowire before and after EBID, respectively. By examining the carbon peaks in Figure 3d,e, it is clearly shown that a carbon layer has been successfully deposited at the end of the nanowire after 15 min of EBID. Some regions without carbon deposition were chosen for indentation tests. It was proved that these carbon layers were strong enough to anchor the nanowires during nanoindentation test.

The peak indentation depths used in this study are less than 20% of the wire diameters. It is generally accepted that the depth of indentation should not exceed 30% of the particle diameter or film thickness to minimize the substrate effect.[21,22] To avoid the sample size effect on nanoindentation mechanical property measurements, the indentation contact radii were smaller than 30% of the nanowire radius.[30]

Parts a, b, and c of Figure 4 show the 3D AFM image of an indentation mark on an $Al_4B_2O_9$ nanowire, cross-sectional height profile, and a representative load-displacement curve,

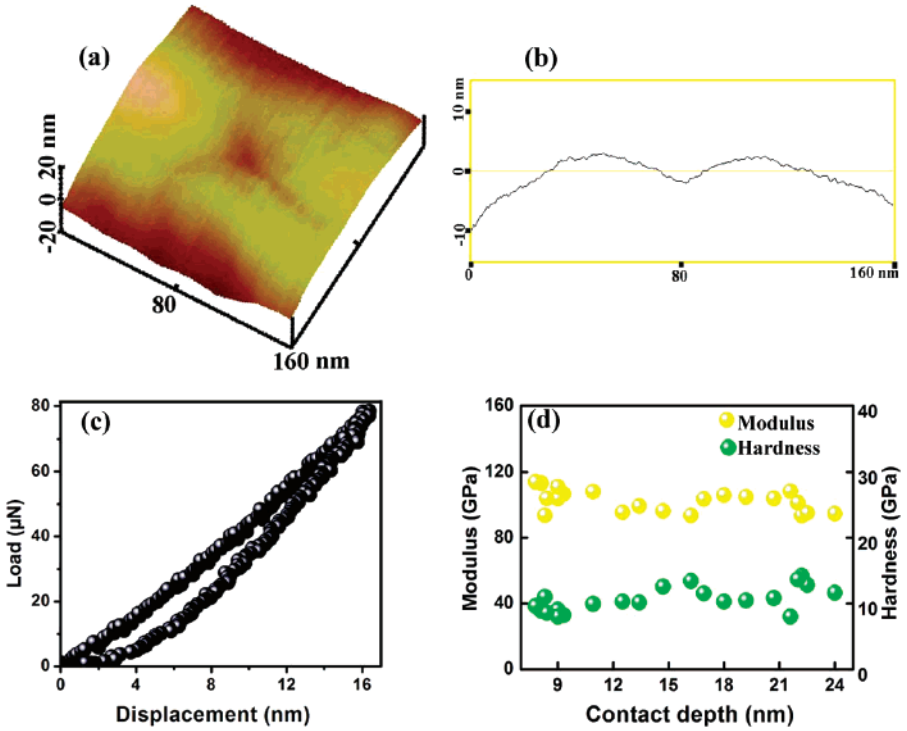

Figure 4. (a) Three-dimensional (3D) AFM image of a nanoindentation impression made on a clamped $Al_4B_2O_9$ nanowire. (b) Cross-sectional height profile of the indentation impression shown in (a). (c) Representative nanoindentation load-displacement curve. (d) Elastic modulus and hardness of $Al_4B_2O_9$ nanowires as a function of indentation contact depth.

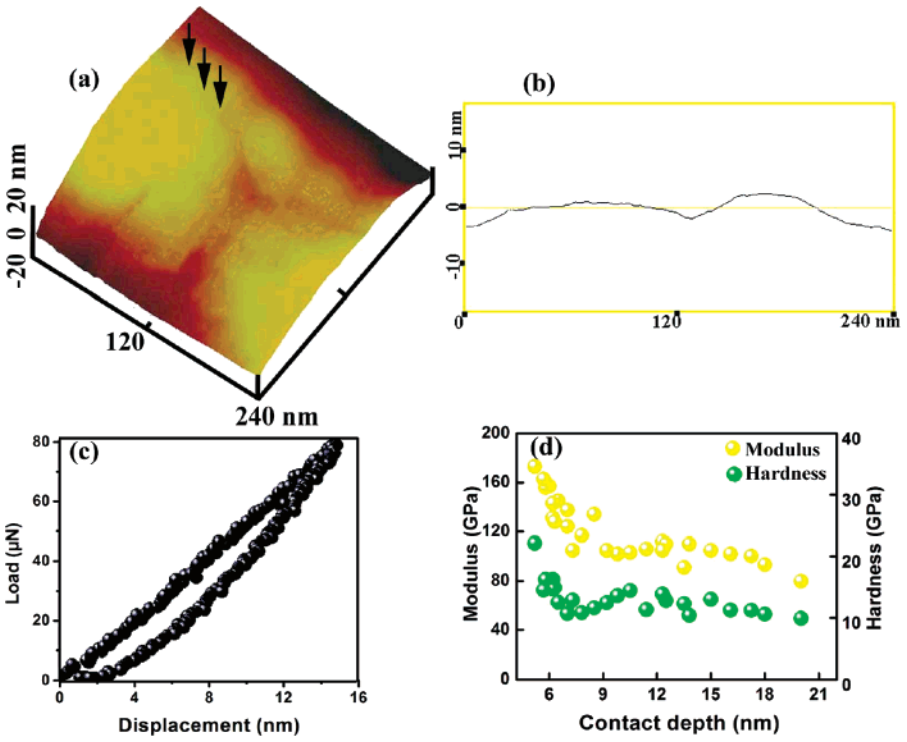

Figure 5. (a) 3D AFM image of a nanoindentation impression made on a clamped $Al_{18}B_4O_{33}$ nanowire. (b) Cross-sectional height profile of the indentation impression shown in (a). (c) Representative nanoindentation load-displacement curve. (d) Elastic modulus and hardness of $Al_{18}B_4O_{33}$ nanowires as a function of indentation contact depth.

respectively. No cracking can be found in the area surrounding the indentation mark in Figure 4a. The hardness and elastic modulus as a function of contact depth are displayed in Figure 4d. The elastic modulus and indentation hardness values of the $Al_4B_2O_9$ nanowires were measured to be 102.8 $\pm$ 1.3 and 10.4 $\pm$ 0.3 GPa, respectively.

Parts a, b, and c of Figure 5 are the 3D AFM image of an indentation mark on an $Al_{18}B_4O_{33}$ nanowire, cross-sectional

height profile, and a representative load-displacement curve, respectively. A noteworthy nanoindentation induced crack can be found in the area surrounding the indentation mark in Figure 5a. As indicated by the arrows in Figure 5a, the crack emanates from one nanoindentation corner. This kind of cracking at high indentation loads may result in a decrease in the measured hardness and elastic modulus, as shown in Figure 5d. The hardness and elastic modulus as a function of contact depth are displayed in Figure 5d. The elastic modulus and hardness values of the $Al_{18}B_4O_{33}$ wires were measured to be 121 ± 4 and 12.8 ± 0.4 GPa, respectively. It can be found that $Al_{18}B_4O_{33}$ nanowires have higher hardness and elastic modulus than $Al_4B_2O_9$ nanowires. Compared with bulk $Al_{18}B_4O_{33}$ with an elastic modulus value of 400 GPa,[31] the modulus of the $Al_{18}B_4O_{33}$ nanowires is decreased approximately by 70%. The low elastic modulus was also observed in other 1D nanomaterials such as ZnO,[32] ZnS,[27] and GaN.[33] Many factors may lead to the reduction of indentation modulus. On one hand, this decrease in modulus can be attributed to the high surface-to-volume ratio of the nanowires.[27] Unlike the atoms locked in the lattice, surface atoms are less constrained, thereby making the nanowire easier to deform in the elastic regime and consequently leading to a lower elastic modulus.[27] On the other hand, the formation of cracks will increase the contact depth, which leads to a lower modulus.

In summary, $Al_4B_2O_9$ and $Al_{18}B_4O_{33}$ nanowires were synthesized via one-step combustion method by controlling the Al:B atomic ratio and growth temperature. Structural characterization indicates that the $Al_4B_2O_9$ and $Al_{18}B_4O_{33}$ nanowires have different growth behavior. The hardness and elastic modulus were measured by directly indenting individual EBID fixed nanowires. The results show that the $Al_{18}B_4O_{33}$ nanowires have higher hardness and elastic modulus than $Al_4B_2O_9$ nanowires. We found a reduction in elastic modulus of $Al_{18}B_4O_{33}$ nanowires compared with their bulk counterpart. These findings are significant for designing aluminum borate nanowire based nanocomposites and nanodevices.

Acknowledgment. Financial support for this study was provided by the National Science Foundation (CMMI-0653651 and EPS-0296165), the ACS Petroleum Research Fund (ACS PRF 40450-AC10), and the University of South Carolina NanoCenter. We thank Dr. Qing Yang (Zhejiang University, China) for valuable discussions.

References

(1) Yang, P. D.; Lieber, C. M. *Science* **1996**, *273*, 1836.
(2) Pan, Z. W.; Dai, Z. R.; Wang, Z. L. *Science* **2001**, *291*, 1947.
(3) Zhu, H. W.; Xu, C. L.; Wu, D. H.; Wei, B. Q.; Vajtai, R.; Ajayan, P. M. *Science* **2002**, *296*, 884.
(4) Huang, Y.; Duan, X. F.; Cui, Y.; Lauhon, L. J.; Kim, K. H.; Lieber, C. M. *Science* **2001**, *294*, 1313.
(5) Zhao, Q.; Zhang, H. Z.; Xu, X. Y.; Wang, Z.; Xu, J.; Yu, D. P.; Li, G. H.; Sun, F. H. *Appl. Phys. Lett.* **2005**, *86*, 193101.
(6) Chen, C. Q.; Zhu, J. *Appl. Phys. Lett.* **2007**, *90*, 043105.
(7) Dong, L. X.; Tao, X. Y.; Zhang, L.; Zhang, X. B.; Nelson, B. J. *Nano Lett.* **2007**, *7*, 58.
(8) Ma, R. Z.; Bando, Y.; Sato, T. *Appl. Phys. Lett.* **2002**, *81*, 3467.
(9) Li, Y.; Fan, Z. Y.; Lu, J. G.; Chang, R. P. H. *Chem. Mater.* **2004**, *16*, 2512.
(10) Zhu, Y. C.; Bando, Y.; Ma, R. Z. *Adv. Mater.* **2003**, *15*, 1377.
(11) Tang, C. C.; Elssfah, E. M.; Zhang, J.; Chen, D. F. *Nanotechnology* **2006**, *17*, 2362.
(12) Zhang, J.; Huang, Y.; Lin, J.; Ding, X. X.; Huang, Z. X.; Qi, S. R.; Tang, C. C. *J. Phys. Chem. B* **2005**, *109*, 13060.
(13) Song, H. S.; Elssfah, E. M.; Zhang, J.; Lin, J.; Luo, J. J.; Liu, S. J.; Huang, Y.; Ding, X. X.; Gao, J. M.; Qi, S. R.; Tang, C. C. *J. Phys. Chem. B* **2006**, *110*, 5966.
(14) Ma, R. Z.; Bando, Y.; Sato, T.; Tang, C.C.; Xu, F. F. *J. Am. Chem. Soc.* **2002**, *124*, 10668.
(15) Song, H. S.; Luo, J. J.; Zhou, M. D.; Elssfah, E. E.; Zhang, J.; Lin, J.; Liu, S. J.; Huang, Y.; Ding, X. X.; Gao, J. M.; Tang, C. C. *Cryst. Growth Des.* **2007**, *7*, 576.
(16) Li, Y.; Chang, R. P. H. *Mater. Chem. Phys.* **2006**, *97*, 23.
(17) McKittrick, J.; Shea, L. E.; Bacalski, C. F.; Bosze, E. J. *Displays* **1999**, *19*, 169.
(18) Cordier, A.; Peigney, A.; Grave, E. D.; Flahaut, E.; Laurent, C. *J. Eur. Ceram. Soc.* **2006**, *26*, 3099.
(19) Ghosh, P.; Mahanty, S.; Raja, M. W.; Basu, R. N.; Maiti, H. S. *J. Mater. Res.* **2007**, *22*, 1162.
(20) Ding, W.; Dikin, D. A.; Chen, X.; Piner, R. D.; Ruoff, R. S.; Zussman, E.; Wang, X. N.; Li, X. D. *J. Appl. Phys.* **2005**, *98*, 014905.
(21) Li, X. D.; Bhushan, B. *Mater. Charact.* **2002**, *48*, 11.
(22) Bhushan, B.; Li, X. D. *Int. Mater. Rev.* **2003**, *48*, 125.
(23) Woodruff, D. *Oxide Surfaces*; Elsevier: New York, 2001; Chapter 12, p 7.
(24) Krist, Z. *Mineral* **1901**, *34*, 449.
(25) Wang, J.; Sha, J.; Yang, Q.; Wang, Y.; Yang, D. *Mater. Res. Bull.* **2005**, *40*, 1551.
(26) Li, X. D.; Gao, H. S.; Murphy, C. J.; Caswell, K. K. *Nano Lett.* **2003**, *3*, 1495.
(27) Li, X. D.; Wang, X. N.; Xiong, Q. H.; Eklund, P. C. *Appl. Phys. Lett.* **2005**, *87*, 233113.
(28) Li, X. D.; Gao, H. S.; Murphy, C. J.; Gou, L. F. *Nano Lett.* **2004**, *4*, 1903.
(29) Li, X. D.; Wang, X. N.; Xiong, Q. H.; Eklund, P. C. *Nano Lett.* **2005**, *5*, 1982.
(30) Xu, Z. H.; Li, X. D. *Acta. Mater.* **2006**, *54*, 1699.
(31) Tjong, S. C.; Jiang, W. *J. Appl. Polym. Sci.* **1999**, *73*, 2247.
(32) Mao, S.; Zhao, M.; Wang, Z. L. *Appl. Phys. Lett.* **2003**, *83*, 993.
(33) Ni, H.; Li, X. D.; Cheng, G. S.; Klie, R. *J. Mater. Res.* **2006**, *21*, 2882.

NL071772X